Theor. Comput. Fluid Dyn. (2016) 30:339–348
DOI 10.1007/s00162-016-0383-z

ORIGINAL ARTICLE

Alexander Yu. Gelfgat

Visualization of three-dimensional incompressible flows by quasi-two-dimensional divergence-free projections in arbitrary flow regions

Received: 26 August 2015 / Accepted: 10 February 2016 / Published online: 24 February 2016

Abstract A visualization of three-dimensional incompressible flows by divergence-free quasi-two-dimensional projections of the velocity field onto three coordinate planes is revisited. An alternative and more general way to compute the projections is proposed. The approach is based on the Chorin projection combined with a SIMPLE-like iteration. Compared to the previous methodology based on divergence-free Galerkin–Chebyshev bases, this technique, formulated in general curvilinear coordinates, is applicable to any flow region and allows for faster computations. To illustrate this visualization method, examples in Cartesian and spherical coordinates, as well as post-processing of experimental 3D-PTV data, are presented.

Keywords Incompressible flow · Flow visualization · Staggered grid

1 Introduction

While visualization of two-dimensional incompressible flows can be easily done by plotting its streamlines, representation of a three-dimensional flow on a two-dimensional graph remains a challenge. Several recent state-of-the-art visualization techniques are discussed in [1–4] to which the reader is referred for details. Here we focus on the method of visualization of three-dimensional incompressible fluid flow proposed in [5]. There, an incompressible velocity field $\boldsymbol{v} = \left(v_x, v_y, v_z\right)$ was visualized by calculating its divergence-free projections onto two-dimensional coordinate planes and computing the corresponding vector potentials which are an extension of the two-dimensional stream function. For calculations of the potentials, a projection on the divergence-free velocity bases satisfying all the boundary conditions was proposed. It was shown how these bases can be built from linear superpositions of the Chebyshev polynomials, and the whole approach was illustrated for two well-known benchmark problems: buoyancy convection in a laterally heated cube and flow in a lid-driven cubic cavity. This approach was recently implemented in [6] to describe steady and time-dependent natural convection flows.

While the Chebyshev-polynomials-based approach can yield an analytic accuracy, it is rather difficult for numerical realization and is restricted to simple domains in the Cartesian coordinates. It is also noticeably CPU-time consuming, which becomes problematic when several tens of time snapshots must be post-processed to be joined in a single animation.

In this article, we propose another approach for calculation of the quasi-two-dimensional divergence-free projections. This approach resembles the idea of SIMPLE iterations [8,9], where the Chorin projection is applied several times within a single time step until the velocity corrections vanish. Here we reformulate this iteration procedure to make it suitable for our purposes, so that the iterations converge to one of the

Communicated by Tim Colonius.

A. Yu. Gelfgat (✉)
School of Mechanical Engineering, Faculty of Engineering, Tel-Aviv University, Ramat Aviv, Tel Aviv 69978, Israel
E-mail: gelfgat@tau.ac.il

projections. The whole iteration procedure is relatively simple. It is argued that in the case of standard central finite difference or finite volume formulations on a staggered grid, a single iteration may result in a vector field with the zero grid divergence. The whole procedure is then generalized for arbitrary curvilinear orthogonal coordinates.

The proposed approach removes previous restrictions to the Cartesian coordinates and simple flow regions. We illustrate this for the problem of buoyancy convection from a hot sphere placed inside a cold cube. The visualization is carried out first in Cartesian coordinates, in which the numerical solution was computed. Then the numerical data are transformed to spherical coordinates, where the whole visualization procedure is repeated. The latter visualization allows for a better understanding of the distortion of the spherical symmetry caused by the cubic walls. To show that the proposed approach can be applied also for three-dimensional experimental data, we visualize results of 3D-PTV measurements of the flow in a shallow embayment.

2 Visualization method and numerical technique

We start with a brief description of the visualization method of Gelfgat [5]. A divergence-free velocity field $\boldsymbol{v} = \left(v_x, v_y, v_z\right)$ is projected onto coordinate planes or surfaces in a way that (1) maintains its two-dimensional divergence equal to zero and (2) preserves the boundary conditions. These projections are described by vector potentials that have only one nonzero component. The latter corresponds to the two-dimensional stream function in a single coordinate plane, so that its 3D isosurface is an extension of the two-dimensional stream line. The projected velocities are tangent to these isosurfaces.

Consider a divergence-free velocity field $\boldsymbol{v}\,(x, y, z)$ in an arbitrary three-dimensional flow region V satisfying some boundary conditions at the region border. Considering a coordinate plane $z = z_0$, we define $\hat{\boldsymbol{v}}^{(z)} = \left(\hat{\boldsymbol{v}}_x, \hat{\boldsymbol{v}}_y, 0\right)$ to be a divergence-free projection of $\boldsymbol{v}$, if it satisfies the same boundary conditions for v_x and v_y, and

$$\langle \boldsymbol{v} - \hat{\boldsymbol{v}}^{(z)},\, \hat{\boldsymbol{v}}^{(z)} \rangle_{(x,y)} = 0, \qquad \nabla_{(x,y)} \cdot \hat{\boldsymbol{v}}^{(z)} = \frac{\partial \hat{\boldsymbol{v}}_x}{\partial x} + \frac{\partial \hat{\boldsymbol{v}}_y}{\partial y} = 0, \tag{1}$$

where

$$\langle \boldsymbol{v}, \boldsymbol{u} \rangle_{(x,y)} = \int_A \boldsymbol{v}\,(x, y, z = z_0) \cdot \boldsymbol{u}\,(x, y, z = z_0)\, \mathrm{d}A \tag{2}$$

and A is the area obtained as a cross-section of the volume V by the plane $z = z_0$. The two-dimensional vector $\hat{\boldsymbol{v}}^{(z)}$ can be described by a stream function $\psi^{(z)}$, which, in its turn, can be interpreted as a single nonzero z-component of its vector potential $\boldsymbol{\Psi}^{(z)}$:

$$\hat{\boldsymbol{v}}^{(z)} = rot\boldsymbol{\Psi}^{(z)}, \quad \boldsymbol{\Psi}^{(z)} = \left(0, 0, \psi^{(z)}\right), \quad \hat{v}_x = \frac{\partial \psi^{(z)}}{\partial y}, \quad \hat{v}_y = -\frac{\partial \psi^{(z)}}{\partial x} \tag{3}$$

Clearly, the isolines $\psi^{(z)} = \text{const}$ are streamlines of the vector $\hat{\boldsymbol{v}}^{(z)}$ in every plane $z = \text{const}$. Computing $\psi^{(z)}$ for different levels of z, e.g., at each grid level of a structured grid, we obtain a scalar three-dimensional function $\psi^{(z)}\,(x, y, z)$ that corresponds to a vector $\hat{\boldsymbol{v}}^{(z)} = \left(\hat{v}_x\,(x, y, z)\,, \hat{v}_y\,(x, y, z)\,, 0\right)$. The latter is called quasi-two-dimensional projection of the initial vector field $\boldsymbol{v}$. At each z level, the isosurfaces of $\psi^{(z)}\,(x, y, z)$ are tangent to the corresponding divergent-free projection $\hat{\boldsymbol{v}}^{(z)}$. Considering similar projections in the $x = \text{const}$ and $y = \text{const}$ planes, we obtain two additional scalar three-dimensional functions $\psi^{(x)}\,(x, y, z)$ and $\psi^{(y)}\,(x, y, z)$ with similar properties. Finally, three sets of isosurfaces of the three functions $\psi^{(x)}$, $\psi^{(y)}$, and $\psi^{(z)}$ complete the visualization of the flow. Examples of such visualizations are given in [5].

As mentioned above, the quasi-two-dimensional projections were calculated in [5] by projecting the initial flow field on the specially built divergence-free basis satisfying all the boundary conditions. For all the technical details, the reader is referred to the above paper and references therein. This approach is straightforward, but quite complicated and CPU-time consuming. Besides, it is limited to simple flow regions. An alternative way to calculate the quasi-two-dimensional projections is proposed below.

It was argued in [5] that application of the Helmholtz-Leray decomposition for computation of quasi-two-dimensional projections, which can be done via the Chorin projection [7], will alter the boundary conditions for the velocity tangent to the boundary. A similar problem arises if, say, $\psi^{(z)}$ is calculated from the Poisson equation $\Delta\psi\,(x, y) = rot_z\,[\boldsymbol{v}\,(x, y, z = z_0)]$. To satisfy no-slip conditions at an arbitrary boundary, it will be necessary to require simultaneously the Dirichlet and Neumann boundary conditions for $\psi^{(z)}$, which will

make the problem unsolvable. In the following, we argue that the Chorin projection combined with the main idea of the SIMPLE iteration [8,9] may yield a correct and accurate result. Thus, for calculation of $\hat{\boldsymbol{v}}^{(z)}$, the following iterative procedure is proposed

Start with $\hat{\boldsymbol{v}}^{(z)} = \boldsymbol{u}_0 = \left(v_x\,(x, y, z = \text{const})\,, v_y\,(x, y, z = \text{const})\,, 0\right)$
Repeat until $\|\varphi\| < \varepsilon$

1. Solve $\Delta_{(x,y)}\varphi = \frac{\partial^2\varphi}{\partial x^2} + \frac{\partial^2\varphi}{\partial y^2} = \nabla_{(x,y)} \cdot \hat{\boldsymbol{v}}^{(z)} = \frac{\partial \hat{v}_x}{\partial x} + \frac{\partial \hat{v}_y}{\partial y}$; $\left[\frac{\partial\varphi}{\partial n}\right]_\Gamma = 0$.
2. Correct $\hat{\boldsymbol{v}}^{(z)}$: $\hat{\boldsymbol{v}}^{(z)} \to \hat{\boldsymbol{v}}^{(z)} - \nabla_{(x,y)}\varphi$, i.e., $\hat{v}_x \to \hat{v}_x - \frac{\partial\varphi}{\partial x}$, $\hat{v}_y \to \hat{v}_y - \frac{\partial\varphi}{\partial y}$
3. Enforce boundary conditions for $\hat{\boldsymbol{v}}^{(z)}$ by correction of its boundary values and go to stage 1.

The above iterative procedure can be applied for any numerical discretization, provided that consecutive application of approximations of the gradient and divergence operators results in the approximation of the Laplacian operator. An extension to general orthogonal curvilinear coordinates is straightforward (see, e.g., Appendix of the book [11]). If the iteration converges, the numerical approximation of the resulting divergence of the velocity field $\hat{\boldsymbol{v}}^{(z)}$ zeroes and the boundary conditions are satisfied. To prove that $\hat{\boldsymbol{v}}^{(z)}$ is the quasi-two-dimensional projection, it is necessary to show that the first equality in (1) holds. Indeed, this equality can be altered by stage 3 of the iteration, so that it will be satisfied only approximately. To argue that the equality holds, we observe that the correction step 2 does not alter the curl of the field, so that if the boundary points do not pose a problem, one can expect $\nabla \times \boldsymbol{u}_0 = \nabla \times \hat{\boldsymbol{v}}^{(z)}$, which makes the difference $(\boldsymbol{u}_0 - \hat{\boldsymbol{v}}^{(z)})$ a potential function. Then the equality $\langle \boldsymbol{v} - \hat{\boldsymbol{v}}^{(z)}, \hat{\boldsymbol{v}}^{(z)}\rangle_{(\boldsymbol{x},\boldsymbol{y})} = \langle \boldsymbol{u_0} - \hat{\boldsymbol{v}}^{(z)}, \hat{\boldsymbol{v}}^{(z)}\rangle_{(\boldsymbol{x},\boldsymbol{y})} = 0$ can be expected due to orthogonality of the potential and solenoidal vector fields [10].

It should be emphasized also that the above iteration procedure is assumed to be applied within a numerical method, so that only the corresponding approximation of the velocity divergence, called grid divergence, can be zeroed. Therefore, the visualizations discussed below can become meaningless on coarse grids, where the numerical approximation error is not sufficiently small.

3 Computation of the projection on a staggered grid

Here we assume that the three-dimensional velocity to be visualized is calculated on a staggered grid. For brevity, we define the staggered grid only in the (x, y) plane and consider only one projection $\hat{\boldsymbol{v}}^{(z)}$. Let x_i, $i = 0, 1, \ldots, M$ and y_j, $j = 0, 1, \ldots, N$ are arbitrarily stretched grid nodes and $x_0 < x_1 < \cdots < x_M$, $y_0 < y_1 < \cdots < y_N$. We define additionally

$$\bar{x}_{i+1/2} = \frac{1}{2}\left(x_i + x_{i+1}\right), \quad i = 0, 1, \ldots, M-1; \quad \bar{x}_{-1/2} = x_0,\ \bar{x}_{M+1/2} = x_M; \tag{4}$$

$$\bar{y}_{j+1/2} = \frac{1}{2}\left(y_j + y_{j+1}\right), \quad j = 0, 1, \ldots, N-1; \quad \bar{y}_{-1/2} = y_0,\ \bar{y}_{N+1/2} = y_N; \tag{5}$$

$$h^{(x)}_{i+1/2} = x_{i+1} - x_i,\ \bar{h}^{(x)}_i = \bar{x}_{i+1/2} - \bar{x}_{i-1/2}, \tag{6}$$

$$h^{(y)}_{j+1/2} = y_{j+1} - y_j,\ \bar{h}^{(y)}_j = \bar{y}_{j+1/2} - \bar{y}_{j-1/2}. \tag{7}$$

The scalar functions are defined in the points $(\bar{x}_{i+1/2}, \bar{y}_{j+1/2})$ and their node values are denoted by the corresponding indices, e.g., scalar potential $\varphi_{i+1/2,j+1/2}$ and $[\nabla_{(x,y)} \cdot \hat{\boldsymbol{v}}^{(z)}]_{i+1/2,j+1/2}$. The $x-$ and $y-$ components of every vector are defined in the points $\left(x_i, \bar{y}_{j+1/2}\right)$ and $\left(\bar{x}_{i+1/2}, y_j\right)$, respectively, and are denoted as $\left[\hat{v}_x\right]_{i,j+1/2}$ and $\left[\hat{v}_y\right]_{i+1/2,j}$. Using central finite differences, we arrive at the following approximations of the gradient, divergence, and Laplacian operators ($i, j > 0$ and $i < M$, $j < N$)

$$\nabla_{(x,y)}\varphi = \left[\frac{\varphi_{i+1/2,j+1/2} - \varphi_{i-1/2,j+1/2}}{\bar{h}^{(x)}_i}\right]_{i,j+1/2} \boldsymbol{e}_x + \left[\frac{\varphi_{i+1/2,j+1/2} - \varphi_{i+1/2,j-1/2}}{\bar{h}^{(y)}_j}\right]_{i+1/2,j} \boldsymbol{e}_y \tag{8}$$

$$\left[\nabla_{(x,y)}\cdot\hat{\boldsymbol{v}}^{(z)}\right]_{i+1/2,j+1/2}=\frac{\left[\hat{v}_x\right]_{i+1,j+1/2}-\left[\hat{v}_x\right]_{i,j+1/2}}{h^{(x)}_{i+1/2}}+\frac{\left[\hat{v}_y\right]_{i+1/2,j+1}-\left[\hat{v}_x\right]_{i+1/2,j}}{h^{(y)}_{j+1/2}} \tag{9}$$

$$\begin{aligned}\left[\Delta_{(x,y)}\varphi\right]_{i+1/2,j+1/2}&=\left[\nabla_{(x,y)}\cdot\left(\nabla_{(x,y)}\varphi\right)\right]_{i+1/2,j+1/2}\\&=\frac{1}{h^{(x)}_{i+1/2}}\left\{\frac{\varphi_{i+3/2,j+1/2}-\varphi_{i+1/2,j+1/2}}{\bar{h}^{(x)}_{i+1}}-\frac{\varphi_{i+1/2,j+1/2}-\varphi_{i-1/2,j+1/2}}{\bar{h}^{(x)}_{i}}\right\}\\&\quad+\frac{1}{h^{(y)}_{j+1/2}}\left\{\frac{\varphi_{i+1/2,j+3/2}-\varphi_{i+1/2,j+1/2}}{\bar{h}^{(y)}_{j+1}}-\frac{\varphi_{i+1/2,j+1/2}-\varphi_{i+1/2,j-1/2}}{\bar{h}^{(y)}_{j}}\right\}\end{aligned} \tag{10}$$

Note that the above approximations are equivalent to the finite volume ones assuming linear interpolation between the grid nodes [9]. At the first step of the above iteration, the problem for the scalar potential φ reduces to equality of the expressions (9) and (10)

$$\left[\Delta_{(x,y)}\varphi\right]_{i+1/2,j+1/2}=\left[\nabla_{(x,y)}\cdot\hat{\boldsymbol{v}}^{(z)}\right]_{i+1/2,j+1/2} \tag{11}$$

at all the inner points, and the boundary conditions are defined by zeroing one-sided finite differences at the borders

$$\varphi_{-1/2,j+1/2}=\varphi_{1/2,j+1/2},\quad \varphi_{M+1/2,j+1/2}=\varphi_{M-1/2,j+1/2} \tag{12}$$

$$\varphi_{i+1/2,-1/2}=\varphi_{i+1/2,1/2},\quad \varphi_{i+1/2,N+1/2}=\varphi_{i+1/2,N-1/2} \tag{13}$$

Considering the result of the correction step 3, we obtain using Eqs. (8)–(11)

$$\begin{aligned}\left\{\nabla_{(x,y)}\cdot\left[\hat{\boldsymbol{v}}^{(z)}-\nabla_{(x,y)}\varphi\right]\right\}_{i+1/2,j+1/2}&=\left[\nabla_{(x,y)}\cdot\hat{\boldsymbol{v}}^{(z)}\right]_{i+1/2,j+1/2}-\left[\nabla_{(x,y)}\cdot\left(\nabla_{(x,y)}\varphi\right)\right]_{i+1/2,j+1/2}\\&=\left[\nabla_{(x,y)}\cdot\hat{\boldsymbol{v}}^{(z)}\right]_{i+1/2,j+1/2}-\left[\Delta_{(x,y)}\varphi\right]_{i+1/2,j+1/2}=0\end{aligned} \tag{14}$$

in all the inner points for $i=1,2,\ldots,M-1$ and $j=1,2,\ldots N-1$. If the boundary conditions are no-slip, the velocity boundary values remain unaltered. Thus, in this particular formulation the iterative process converges to the zero grid-divergence vector field already after the first iteration. Clearly, it is a consequence of keeping the operator equality $div\,[grad\varphi]=\Delta\varphi$, or $\nabla_{(x,y)}\cdot\left(\nabla_{(x,y)}\right)=\Delta_{(x,y)}$ in the present notation, in the approximations (8)–(10). It seems that the same conclusion can be made for any other numerical method that preserves the above operator equality. However a problem may arise in the next-to-the-boundary nodes if the potential boundary values are involved in the approximation of the Laplacian operator. Here it can be easily seen that the boundary values defined by Eqs. (11) and (12) are not involved in the approximation of the gradient and Laplacian operators (8) and (10). This nice property is discussed in [9] in connection with the SIMPLE iteration technique. Here it allows us to obtain the quasi-two-dimensional projections within a single iteration. A problem of altered boundary values appears, for example, for finite difference formulations on a single (not staggered) grid.

Furthermore, since within the above approximation $\boldsymbol{u}_0=\hat{\boldsymbol{v}}^{(z)}+\nabla\varphi$ after the first iteration, the first equality of (1) yields

$$\langle\boldsymbol{v}-\hat{\boldsymbol{v}}^{(z)},\,\hat{\boldsymbol{v}}^{(z)}\rangle_{(\boldsymbol{x},\boldsymbol{y})}=\langle\boldsymbol{u_0}-\hat{\boldsymbol{v}}^{(z)},\,\hat{\boldsymbol{v}}^{(z)}\rangle_{(\boldsymbol{x},\boldsymbol{y})}=\langle\nabla\varphi,\,\hat{\boldsymbol{v}}^{(z)}\rangle_{(\boldsymbol{x},\boldsymbol{y})}=0, \tag{15}$$

where the last equality follows from the orthogonality of potential and solenoidal vector fields. To make it correct within the numerical method, the inner product has to be calculated by a quadrature formula that preserves the finite difference analog of the Gauss theorem. Therefore, within apparent numerical and accuracy restrictions, the vector $\hat{\boldsymbol{v}}^{(z)}$ obtained via the staggered grid approximation and the single iteration is the required quasi-two-dimensional projection of the initial velocity field.

Since calculations for the visualization purposes can usually be coarser than computation of the flow, it is possible to interpolate any experimental or numerical result on a staggered grid and then calculate the three quasi-two-dimensional projections via a robust and straightforward numerical procedure.

4 Examples of flows visualization

At the first stage of verification of the proposed technique of calculation of the quasi-two-dimensional velocity projections, we repeated visualizations of [5] for convection and lid-driven flows in a cubic box. The results were identical to those of [5]. We confirmed also that all the projections are calculated correctly in a single iteration since all the visualized results were obtained on staggered grids.

Below we show an example of flow computed in Cartesian coordinates and visualized in Cartesian, as well as in curvilinear coordinates after the corresponding coordinate and velocity transformations. Since the following examples have a mainly illustrative purpose, we do not focus on details of numerical simulations. At the same time, for possible comparison purposes, we report minimal, maximal and plotted level values of functions shown in the graphs. The second example illustrates visualization of 3D experimental data.

4.1 Air convection from a hot ball inside a cold square box

Consider air convection from a hot isothermal sphere placed in the center of a cubic box with cold walls. The dimensionless radius of the sphere is 0.2, and the dimensionless box length is 1. Formulation of the problem and dimensionless parameters are given in [12,13]. The numerical solutions of Gulberg and Feldman [13] are used for the following visualization. The computations were performed on 100^3 and 200^3 finite volume grids. The finite volume method was combined with the immersed boundary technique to describe the spherical boundary. Since the flows were computed on a Cartesian grid, their visualization in Cartesian coordinates is carried out first and is shown in Fig. 1 for two values of the Rayleigh number, 10^4 and 10^6. For computations of the quasi-two-dimensional projections, we apply the proposed iterative procedure so that no-slip boundary conditions on the sphere are enforced at stage 3. Note that at the end of each iteration step, the staggered finite volume grid yields correct boundary conditions at the box boundaries. However, no-slip conditions at the spherical boundary are satisfied only at the end of the iteration process. The iterations were considered converged when the absolute value of the potential φ was less than 10^{-8} pointwise. After the iterations converged, we examined the first equation of (1) using the finite-volume-based quadrature formula, e.g.,

$$\max \left| \langle \boldsymbol{v} - \hat{\boldsymbol{v}}^{(z)},\, \hat{\boldsymbol{v}}^{(z)} \rangle_{(x,y)} \right| \approx \max_k \left| \sum_{i=0}^{M} \sum_{j=0}^{N} \left\{ \left[\left(v_x - \hat{v}_x \right) \hat{v}_x \right]_{i,j+1/2,k+1/2} \bar{h}_i^{(x)} h_{j+1/2}^{(y)} \right. \right.$$
$$\left. \left. + \left[\left(v_y - \hat{v}_y \right) \hat{v}_y \right]_{i,j+1/2,k+1/2} \bar{h}_j^{(y)} h_{i+1/2}^{(x)} \right\} \right| \tag{16}$$

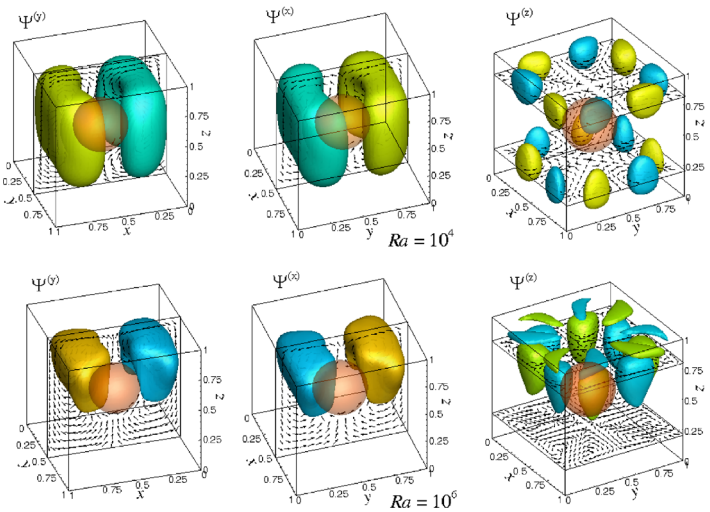

	Ra=10^4	Ra=10^6
$\min \Psi^{(y)}, \max \Psi^{(y)}$	±0.0177	±0.029
$\min \Psi^{(x)}, \max \Psi^{(x)}$	±0.0177	±0.029
$\min \Psi^{(z)}, \max \Psi^{(z)}$	±0.00099	±0.0026
levels of $\Psi^{(y)}$	±0.006	±0.015
levels of $\Psi^{(x)}$	±0.006	±0.015
levels of $\Psi^{(z)}$	±0.0005	±0.001

Fig. 1 Visualization of convective flow of air from a hot sphere placed in the center of a cold cubic box at $Ra = 10^4$ (*upper frames*) and $Ra = 10^6$ (*lower frames*). Translucent *red* surface shows border of the sphere. Isosurfaces of $\Psi^{(y)}$, $\Psi^{(x)}$and $\Psi^{(z)}$ are shown by *colors* and are superimposed with the corresponding vector plots of quasi-two-dimensional projections of velocity fields (color figure online)

The calculations showed that we needed about 120 and 80 iterations to converge in the cases of 100^3 and 200^3 grids, respectively. The lesser number of iterations needed for the finer grid can be explained by a shorter distance between the sphere surface and grid points, so that enforcement of the no-slip condition on the sphere lesser altered the divergence-free field obtained at the second iteration stage. After iterations converged, absolute values of the integrals (15) were below 10^{-15}, which confirms the correctness of computed projections within the numerical model.

The potential isosurfaces are shown in color in Fig. 1, and quasi-two-dimensional projection vectors by black arrows. It is clearly seen that these vectors are tangent to the potential isosurfaces, as expected. Since the flow is symmetric with respect to 90° rotation around the vertical axis, the potentials $\Psi^{(x)}$ and $\Psi^{(y)}$ transform one into another by this rotation. The potential $\Psi^{(z)}$ shows the fluid motion in the (x,y) planes that results into 8 circulating structures and represent the "horizontal" part of the convective ascending/descending flow, which is caused by viscous friction at the spherical and cubic boundaries.

To examine how the spherical symmetry is distorted by the cubic walls, we transform the result into spherical coordinates (R, θ, ϕ) with the pole placed in the cube center. Then we follow the procedure of Sect. 3 to compute three vector potentials $\Psi^{(\phi)}$, $\Psi^{(R)}$, and $\Psi^{(\theta)}$ shown in Fig. 2. Now the no-slip conditions on the sphere are satisfied at the end of each iteration, while the boundary conditions on the square walls must be enforced. Note that if the whole problem was spherically symmetric (e.g., convection between two concentric spheres), one would expect to obtain a ϕ-independent flow with $v_\phi = 0$. Then the potential $\Psi^{(\phi)}$ would depend only on R and θ, and its isolines in cross-sections $\phi = \text{const}$ would coincide with the flow streamlines. When the spherical symmetry is perturbed, the result becomes ϕ dependent. This distortion is clearly represented by the isosurfaces of $\Psi^{(\phi)}$ (Fig. 2) that lose spherical symmetry, but remain symmetric with respect to the 90° rotation around the vertical axis, as is prescribed by the problem symmetry. Two other potentials $\Psi^{(R)}$ and $\Psi^{(\theta)}$ also preserve this symmetry (Fig. 2). They represent projections of the flow field onto spheres $R = \text{const}$ and onto cones $\theta = \text{const}$, which is illustrated in Fig. 3.

Projections of the velocity vectors on a representative plane $\phi = \phi_0$ and $\phi = \phi_0 + \pi$ are plotted in Fig. 3a, where two nonzero components of the velocity projection are shown by arrows. It is clearly seen that the projected velocity is tangent to the plotted isosurface of the potential $\Psi^{(\phi)}$. This projection corresponds to the flow ascending near the hot ball and descending near the cold walls. In spite of all the results obtained in the Cartesian coordinates, one frame in Fig. 3a appears to be more informative than the two frames corresponding to the potentials $\Psi^{(x)}$ and $\Psi^{(y)}$ in Fig. 1. Comparing two frames in Fig. 3a, we observe also that with an increase of the Rayleigh number, the influence of the box boundaries becomes stronger, so that the isosurfaces tend to be parallel to the walls.

Figure 3b, c provide an additional insight on how the spherical symmetry is destroyed. The absence of spherical symmetry at the outer boundaries leads to appearance of a circulating motion, as it was already

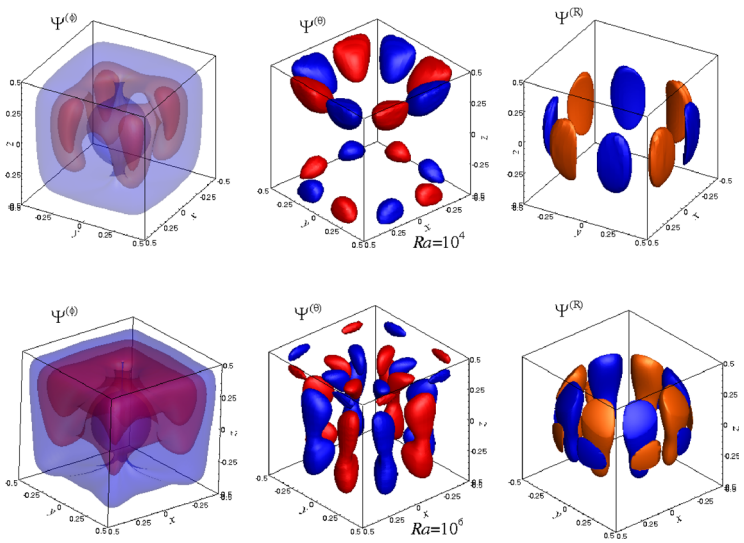

	Ra=10^4	Ra=10^6
min $\Psi^{(\phi)}$, max $\Psi^{(\phi)}$	0, 0.0188	0, 0.0282
min $\Psi^{(\theta)}$, max $\Psi^{(\theta)}$	±0.000941	±0.00140
min $\Psi^{(R)}$, max $\Psi^{(R)}$	±0.00566	±0.00473
levels of $\Psi^{(\phi)}$	0.001, 0.01, 0.015	0.001, 0.01, 0.02
levels of $\Psi^{(\theta)}$	$\pm 3\cdot 10^{-4}$	$\pm 8\cdot 10^{-4}$
levels of $\Psi^{(R)}$	±0.003	±0.0015

Fig. 2 Visualization of convective flow of air from a hot sphere placed in the center of a cold cubic box at $Ra = 10^4$ (*upper frames*) and $Ra = 10^6$ (*lower frames*). Isosurfaces of $\Psi^{(\phi)}$, $\Psi^{(\theta)}$ and $\Psi^{(R)}$ calculated after the data were transformed from the Cartesian grid to the spherical coordinates

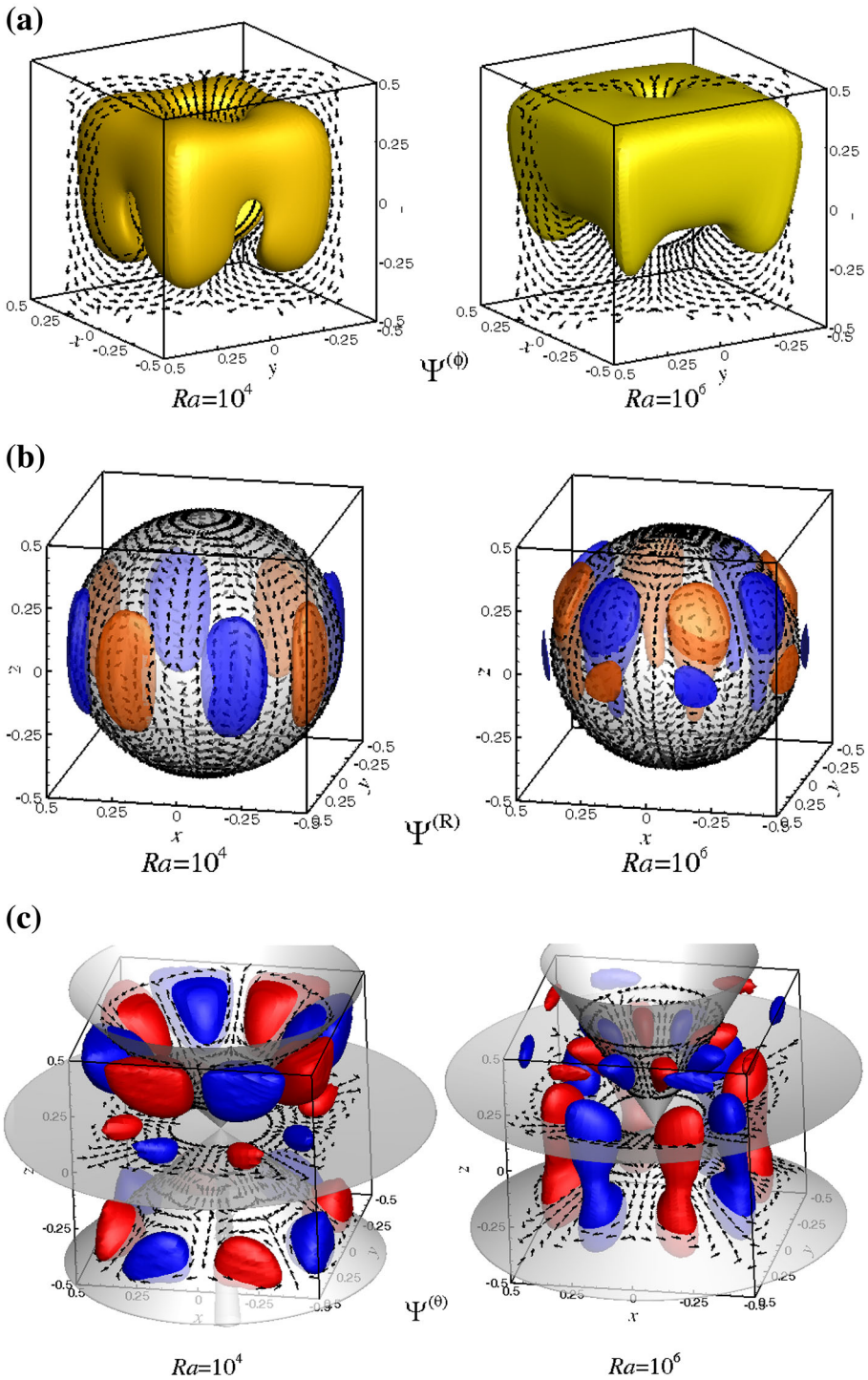

Fig. 3 a Visualization of convective flow of air from a hot sphere placed in the center of a cold cubic box. A characteristic isosurface of $\Psi^{(\phi)}$ with the corresponding vector plots of quasi-two-dimensional projections of velocity fields on the coordinate surfaces $\phi = 0$ and π. **b** Visualization of convective flow of air from a hot sphere placed in the center of a cold cubic box. A characteristic isosurface of $\Psi^{(R)}$ with the corresponding vector plots of quasi-two-dimensional projections of velocity fields on the coordinate surfaces $R = \text{const}$. **c** Visualization of convective flow of air from a hot sphere placed in the center of a cold cubic box. A characteristic isosurface of $\Psi^{(\theta)}$ with the corresponding vector plots of quasi-two-dimensional projections of velocity fields on the coordinate surfaces $\theta = \text{const}$

observed in the horizontal planes in Fig. 1. This circulating motion is decomposed into one located on the spheres $R = \text{const}$ (Fig. 3b) and another one located on the cones $\theta = \text{const}$. Again, we can point to interesting changes in the potential and velocity projections patterns that arise with increasing Rayleigh number. Thus, at a relatively low Rayleigh number, $Ra = 10^4$, the isosurfaces of $\Psi^{(R)}$ lie on the coordinate surface $R = \text{const}$ (Fig. 3b). At larger $Ra = 10^6$, the lower parts of the $\Psi^{(R)}$ isosurfaces are shifted "inside" the coordinate surface, on which we observe two recirculations instead of one. The change of the $\Psi^{(\theta)}$ pattern is even more drastic (Fig. 3c). At $Ra = 10^4$, we observe positive-valued (red) and negative-valued (blue) isosurfaces located one above another in the upper and lower parts of the box. The corresponding direction of recirculating motion is opposite on positive and negative isosurfaces. At $Ra = 10^6$, the patterns of positive and negative isosurfaces change qualitatively, so that at a fixed polar angle ϕ, we observe either positive or negative values of the potential $\Psi^{(\theta)}$. Thus we notice that at cross-sections $\phi = \text{const}$ in the right frame of Fig. 3c, the recirculating motion has the same direction along all values of R and θ.

The difference between usual vector plots and the present approach is illustrated additionally in Fig. 4 showing a midplane $y = 0$ of the cube. In this figure, we compare vectors constructed from the calculated x- and z-velocity components with the isolines of the vector potentials $\Psi^{(y)}$ and $\Psi^{(\phi)}$. Theoretically, the isolines of both potentials must coincide, since they represent the divergence-free projection of the same velocity field on the same plane. After all the calculations are completed they appear to be slightly different because of numerical errors introduced during transformation of velocities from Cartesian to spherical coordinates, as well as due to differences in grid divergence calculated in two different coordinate systems and zeroing approximate max fluxes through different mesh cells. It is clearly seen that the computed, not divergence-free vectors show a different picture of motion in this plane, especially in its upper part.

4.2 Visualization of 3D-PTV experimental data in a shallow embayment

For the third example, we visualize three-dimensional experimental data. The experiment [14] sketched in Fig. 5 was conducted in a shallow embayment that mimicked a similar flow in a river. The experimental "embayment" is 240 mm long (x-direction) and is 240 mm wide (y-direction) and its depth is 30 mm (z-direction). The Reynolds number based on the water depth and the free-stream velocity is $Re = 3900$. In the course of the experiment, three components of the velocity field were measured based on the particle displacements and interpolated on a regular three-dimensional grid with 49 nodes in the $x-$ and $y-$ directions, and 16 nodes in the $z-$direction. The experimental data were then interpolated onto a 40^3 staggered grid, after which the visualization procedure was carried out.

Examining the calculated vector potentials and the corresponding vector plots (Fig. 5b, d), we see that the main flow circulation in the (x, y) planes (Fig. 5b) is represented rather well, and isosurfaces of $\Psi^{(z)}$ clearly describe its pattern. The two other vector potentials describe three-dimensional additions to the quasi-

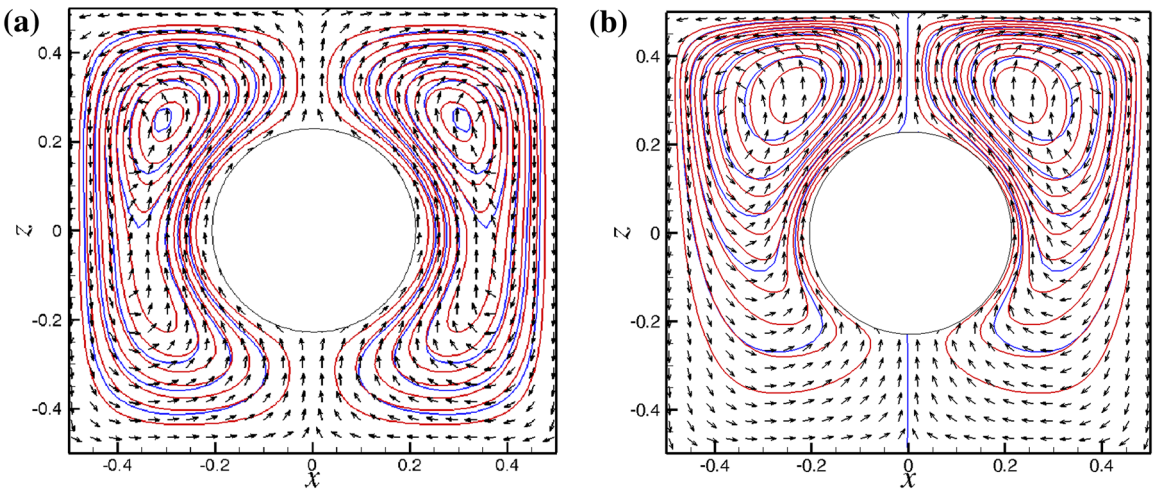

Fig. 4 Visualization of convective flow of air from a hot sphere placed in the center of a cold cubic box in a cross-section $y = 0$. **a** Isolines of vector potentials $\Psi^{(y)}$ (*blue*) and $\Psi^{(\phi)}$(*red*), and 2D vectors built from the calculated Cartesian components v_x and v_z. **a** $Ra = 10^4$, **b** $Ra = 10^6$ (color figure online)

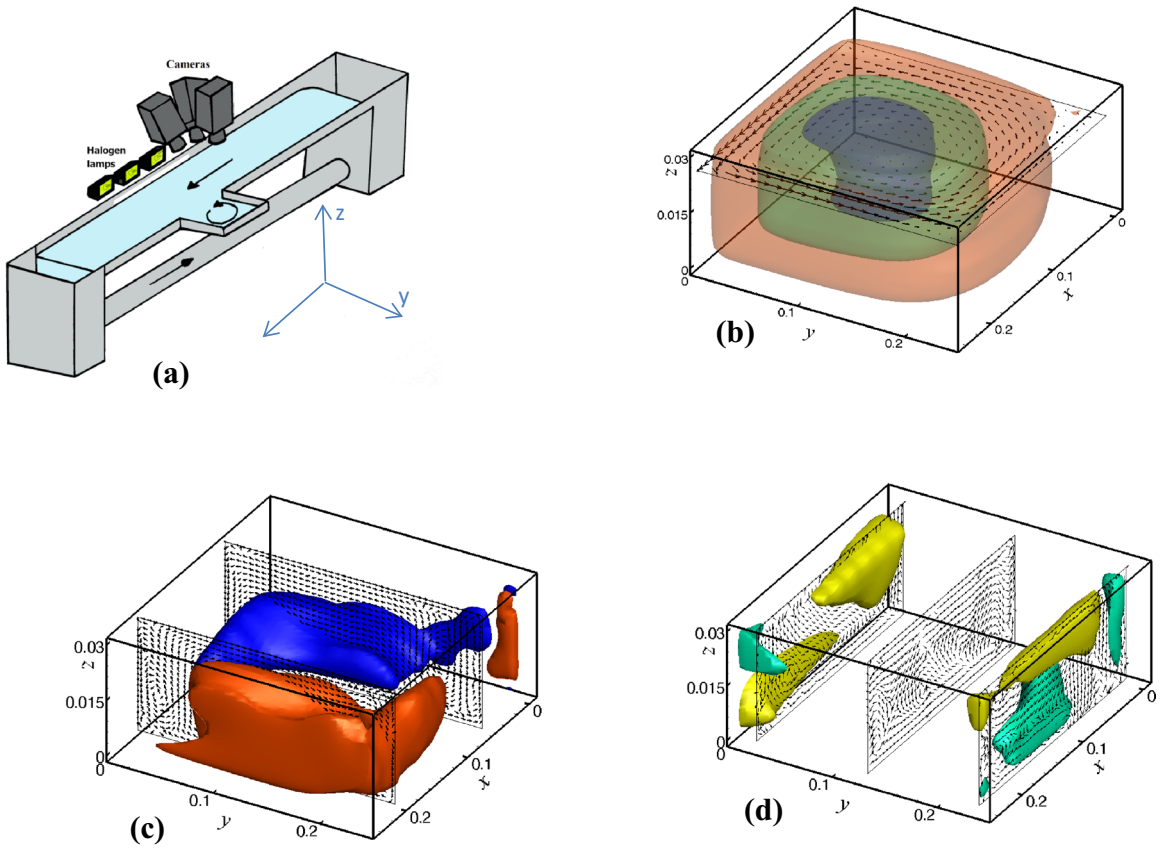

$\min \Psi^{(x)}, \max \Psi^{(x)}$	-0.00026, 0.00060
$\min \Psi^{(y)}, \max \Psi^{(y)}$	-0.00035, 0.00041
$\min \Psi^{(z)}, \max \Psi^{(z)}$	-0.0081, 0.00049
levels of $\Psi^{(x)}$	±0.0001
levels of $\Psi^{(y)}$	-0.0001, 0.00015
levels of $\Psi^{(z)}$	-0.0008, -0.005, -0.007

Fig. 5 Post-processing of experimental results on the flow in a shallow embayment. **a** Sketch of the experimental setup. **c**, **d** Vector potentials and the corresponding *arrow plots* calculated using experimental 3D-PTV data

2D circulation of Fig. 5b. Comparing maximal and minimal values of the three potentials, we observe that maximal absolute value of the potential $\Psi^{(z)}$ is more than an order of magnitude larger than that of the two other potentials, which are comparable in magnitude. This shows that the main circulation carries most of the flow energy. In addition, we observe that circulations in the (y, z) planes (Fig. 5c) are noticeable in the whole bulk of the flow and change in their direction is different for upstream and downstream values of x. The circulations in the (x, z) planes (Fig. 5d) are most intensive near the embayment edges $y = 0$ and 0.25, where the isosurfaces are plotted. There are also weaker circulations in the central part of the embayment, but to make them visible we had to plot arrows of the same length, which does not allow one to estimate relative velocity magnitudes. It should be emphasized, however, that the plots in Fig. 5c, d are based on 11 experimental points along the z direction, which can be insufficient for an accurate numerical post-processing. These two results are yet to be verified either by computation or by more representative experimental data.

5 Conclusions

In this article, we presented an alternative method for computation of quasi-two-dimensional velocity projections needed for visualization of three-dimensional incompressible flows, as it was proposed in our earlier paper [5]. The method is based on the SIMPLE-like iteration and removes previous restrictions on the shape of the flow region and system of coordinates. It is shown also that for the standard finite volume formulation on the staggered grid, the proposed approached may converge in a single iteration.

The proposed method is illustrated on two types of calculated or measured velocity fields and visualized in Cartesian and spherical coordinates. In each case, the visualization allowed us detect some flow features that were not noticed on standard velocity or vorticity plots. This visualization approach is suitable for visualization not only of numerical, but also of experimental data, as is shown by the last example.

Acknowledgments The author wishes to express his gratitude to Yuri Feldman and Yulia Akutina for providing their numerical and experimental data that were used in the above examples.

References

1. McLaughlin, T., Laramee, R.S., Peikert, R., Post, F.H., Chen, M.: Over two decades of integration-based, geometric flow visualization. Comput. Gr. Forum **29**, 1807–1829 (2010)
2. Edmunds, M., Laramee, R.S., Chen, G., Max, N., Zhang, E., Ware, C.: Surface-based flow visualization. Comput. Gr. **36**, 974–990 (2012)
3. Etien, T., Nguyen, H., Kirby, R.M., Siva, C.T.: "Flow visualization" juxtaposed with "visualization of flow": synergistic opportunities between two communities. In: Proceedings of 51st AIAA Aerospace Science Meeting, New Horizon Forum Aerospace Exp., pp. 1–13 (2013)
4. Schulze, M., Martinez Esturo, J., Günther, T., Rössl, C., Seidel, H.-P., Weinkauf, T., Theisel, H.: Sets of Globally Optimal Stream Surfaces for Flow Visualization. Comput. Gr. Forum **33**, 1–10 (2014)
5. Gelfgat, A.Yu.: Visualization of three-dimensional incompressible flows by quasi-two-dimensional divergence-free projections. Comput. Fluids **97**, 143–155 (2014)
6. Gelfgat A.Yu.: Oscillatory instability of three-dimensional natural convection of air in a laterally heated cubic box, submitted for publication. (2015). arXiv:1508.00652
7. Chorin, A.J.: Numerical solution of the Navier–Stokes equations. Math. Comput. **22**, 745–762 (1968)
8. Patankar, S.V., Spalding, D.B.: A calculation procedure for heat, mass and momentum transfer in three-dimensional parabolic flows. Int. J. Heat Mass Transf. **15**, 1787–1806 (1972)
9. Patankar, S.V.: Numerical Heat Transfer and Fluid Flow. Taylor & Francis, Washington, DC (1980)
10. Kopachevsky, M.D., Krein, S.D.: Operator Approach to Linear Problems of Hydrodynamics. Springer, Berlin (2000)
11. Batchelor, G.K.: An Introduction to Fluid Dynamics. Cambridge University Press, Cambridge (2000)
12. Yoon, H.S., Yu, D.H., Ha, M.Y., Park, Y.G.: Three-dimensional natural convection in an enclosure with a sphere at different vertical locations. Int. J. Heat Mass Transf. **53**, 3143–3155 (2010)
13. Gulberg, Y., Feldman, Y.: On laminar natural convection inside multi-layered spherical shells. Int. J. Heat Mass Transf. **91**, 908–921 (2015)
14. Akutina, Y.: Experimental investigation of flow structures in a shallow embayment using 3D-PTV. PhD thesis, McGill University, Montreal, QC (2015)